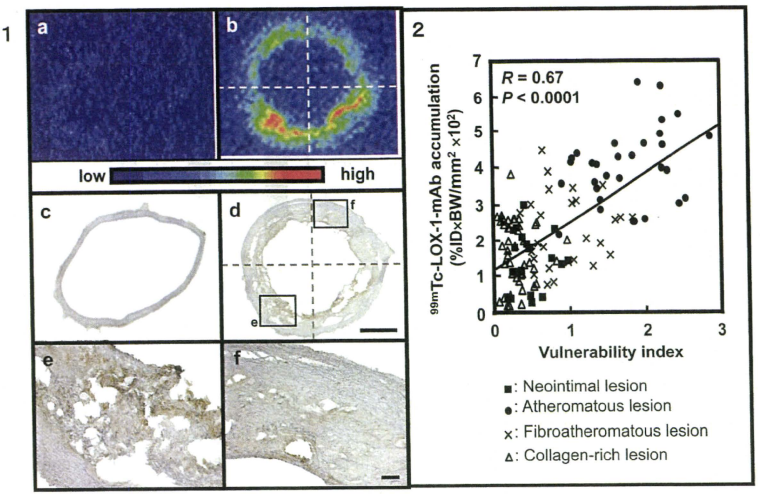

図4　1: WHHLMIウサギでの^{99m}Tc-抗LOX抗体の血管壁への分布と血管壁でのLOX-1の発現，2: プラークの不安的指標（vulnerability index）と^{99m}Tc-抗LOX抗体の集積量との関係

a,c: コントロールウサギ，b,d,e,f: WHHLMIウサギ，a,b: ^{99m}Tc-抗LOX抗体投与後のオートラジグラフィ，c,d,e,f: 免疫組織化学的染色．

$$\text{Vulnerability index} = \frac{\text{不安定因子の面積（マクロファージ＋細胞外脂質）}}{\text{安定化因子の面積（平滑筋細胞＋コラーゲン線維）}}$$

LDLの取り込みを介することで，血管内皮細胞に細胞接着因子，白血球遊走因子などの発現を誘導すること，ii) マクロファージにおいて酸化LDLを取り込み，その泡沫化に寄与すること，iii) 平滑筋細胞のアポトーシスを誘導すること，iv) Matrix metalloproteinase（MMP）の発現を介して細胞外マトリックスの分解を促進することなど，酸化LDLの取り込みを介して動脈硬化プラークの進展および不安定化に深く関与している可能性が報告されている（図1）．

そこで，不安定性動脈硬化プラークの分子イメージングの標的としてのLOX-1の有効性の検討が計画され，WHHLMIウサギを用いて，動脈硬化プラークの不安定性とLOX-1の発現とが高い相関を示すことが見出されている[17]（図4）．さらにこの結果に基づいて，LOX-1を標的とする放射性分子プローブとして，LOX-1の細胞膜外領域に抗原認識部位を有する抗LOX-1抗体に^{99m}Tcを結合させた^{99m}Tc標識抗LOX-1抗体を合成し，WHHLMIウサギを用いたイメージングにおいて，コントロールウサギに比較して明瞭に大動脈をイメージングできること，また，その各病変における放射能集積量は動脈硬化プラークの組織学的な不安定性の指標と高く相関することが認められており（図4），その不安定プラーク部位への集積の特異性は^{18}F-FDGよりも高いことが報告

されている[18]．また，抗LOX-1抗体を表面に結合し，内部に放射性同位元素（^{111}In），ガドリニウム，蛍光色素を内包した，ナノ粒子リポソームを作成し，apoEノックアウトマウス（apoE KO）およびLDL受容体欠損マウスにおいてマルチモダルイメージングを行い，MRI，光イメージングと一致して，動脈硬化部位をRIでイメージすることに成功している[19]．さらに，そのRI集積部位はLOX-1の発現，マクロファージの集積，アポトーシス，MMP-9の発現が認められており，このLOX-1を標的とするプローブが動脈硬化不安定プラークのイメージングに有効性であることが示されている[19]．

D. アポトーシスを標的としたイメージング

動脈硬化の不安定化の過程において，マクロファージ（泡沫細胞）のアポトーシスは脂質コアの形成に寄与し，一方，平滑筋細胞のアポトーシスは細胞外マトリックス形成を抑制して線維性被膜を脆弱化させることから（図1），不安定性動脈硬化プラークのイメージングに，アポトーシスのイメージングプローブ，^{99m}Tc-Annexin A5の使用が多数試みられている[20,21]．Annexin A5は，細胞がアポトーシスを起こす際に細胞膜の脂質二重膜内から膜外へと表れるホスファチジルセリンに対して強い結合性を有しており，この分子に^{99m}Tcを結合したものが^{99m}Tc標識Annexin A5である．不安定プラークのイメージングにおいては，^{99m}Tc-Annexin A5は^{18}F-FDGよりも標的部位への集積の特異性が高いことが報告されている．さらに，^{99m}Tc-Annexin A5の動脈硬化プラークへの取り込みは，カスパーゼ阻害剤によるアポトーシス抑制に基づく不安定プラークの治療効果を評価するために有効であることも示されている[20]．このようなアポトーシスの標的としての有効性の評価とともに，プローブとして高分子化合物^{99m}Tc-Annexin A5よりも臨床応用が容易な低分子化合物のプローブの開発も進められており，^{18}F-イサチン誘導体などが報告されている[22]．

E. Metalloproteinaseを標的としたイメージング

Matrix metalloproteinase（MMP）は血管の炎症およびリモデリングに重要な役割を果たしており，血管が障害時には，炎症性刺激により活性化される．これが血管内膜の粥腫線維性被膜のタンパク質を分解し，それを脆弱化して，血栓形成に結びつく（図1）．したがって，動脈硬化プラークでのMMP活性を測定することは，そのプラークの不安定性を評価することができると考えられる．そこで，MMPを標的とした不安定プラークイメージングプローブの開発が注目され，主に3つのアプローチが試みられている．

1つは，MMPの基質を放射性核種で標識したプローブで，活性化されたMMPによって分解され，分解後細胞内にとどまるというものである．2つ目はMMP阻害剤を放射性核種で標識したプローブで，^{99m}Tc-RP805（MPI）や^{111}In-RP782などが開発され，粥状動脈硬化症のモデル動物であるapoE KOマウスを用いてイメージングが試みられ，血管壁への放射能の集積が正常マウスに比べてapoE KOマウスでは有意に高いことが報告されている[23,24]．さらに，^{99m}Tc-RP805の集積はMMP2，MMP9，マクロファージの発現と相関しており[23]，MMPの発現を抑制する治療における治療効果の評価に有効であることも報告されている[25]．また，粥状動脈硬化が進行し，頸動脈にまで拡大しているapoE KOマウス の大動脈血管では，MMPファミリーのMMP2，MMP9の発現がカスパーゼ陽性細胞の存在パーセント，

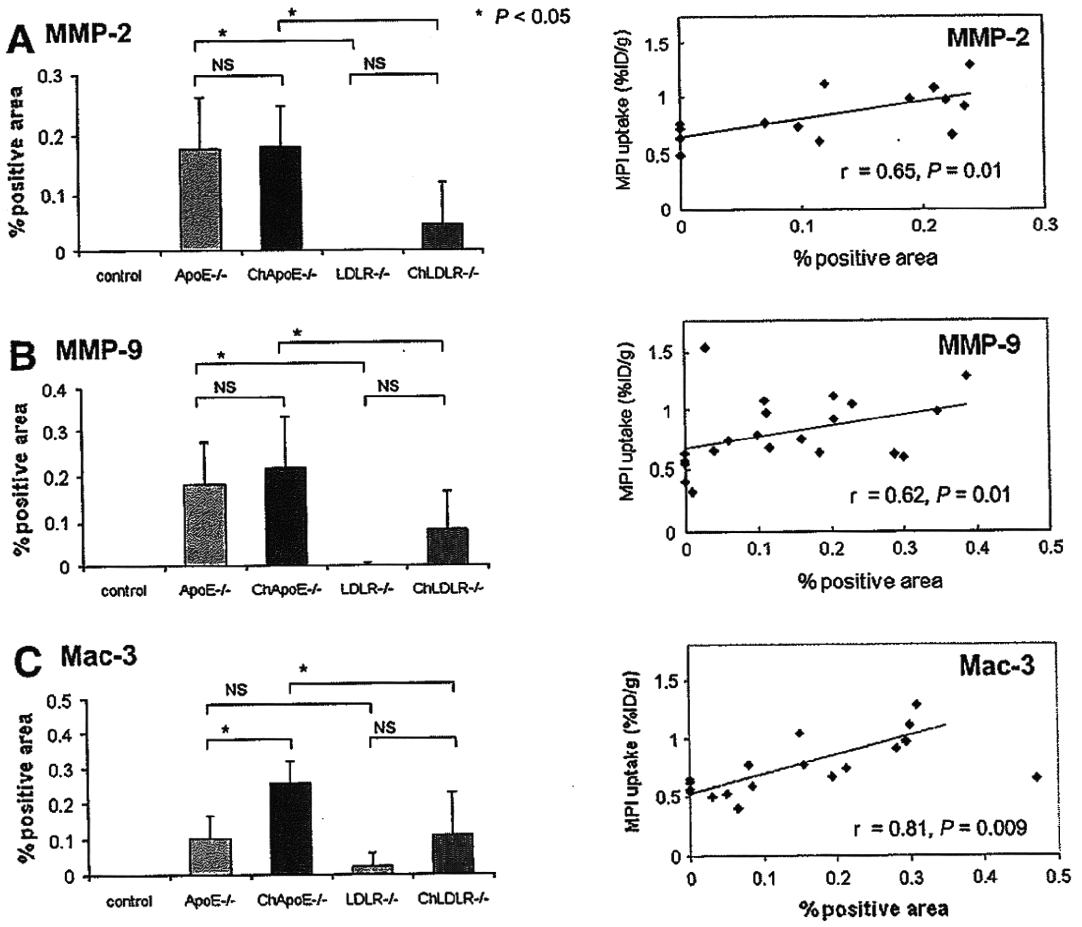

図5　動脈硬化モデルマウス（アポEノックアウトマウスApoE$^{-/-}$およびLDL受容体欠損マウスLDL$^{-/-}$）の動脈血管壁における^{99m}Tc-MPIの取り込みとMMP-2，MMP-9，マクロファージ発現との関係（Ch: 高コレステロール食）[21]

すなわちアポトーシスの割合よりも高いこと[23]（図5），そのためにアポトーシスイメージングプローブ^{99m}Tc-Annexin A5と比較した場合，^{99m}Tc-RP805の方が疾患がより進んでいる状態でのイメージングに有効であると推測されている[26]．さらに，^{99m}Tc-RP805は，^{18}FDGとは異なり，心筋細胞には集積せず，高いS/N比が得られることも報告されている[3]．3つ目は，細胞膜に存在するMMP（MMP14，MT1-MMP）に対する抗体の標識体を用いるもので，その標的部位への集積は他のプローブに比べてかなり特異性が高いことが報告されている[27]．これらのことから，不安定プラークのイメージングの標的としてMMPが有効であること，そして^{99m}Tc-RP805のようなMMP阻害剤の標識体が不安定プラークのイメージングプローブとして有効であることが示されている．

F. その他のイメージング

上記以外に，プラークの形成の最初の段階で血管内皮にLDLが取り込まれることからLDLの標

識体，炎症反応に関与するインターロイキンIL-2[28]，単球に対する走化因子であるケモカインMCP-1（monocyte chemoattractant protein-1）の標識体[29]，心筋梗塞後の心筋リモデリングにおける心筋線維化の存在とその線維形成の程度の評価を目的とした細胞接着分子に結合するRGD構造を基本とするペプチドCRIP（Cy5.5-RDG imaging peptide）の^{99m}Tc標識体[30]など，多くの分子プローブの開発研究およびそれを用いた分子イメージング研究が活発に展開されている．さらに，基材としてナノ粒子を利用する分子プローブの開発も盛んに行われており，核医学イメージングをはじめ[31]，磁気共鳴イメージング（MRI）[32-40]，光イメージング[19]などを対象に研究が活発に進められている．

むすび

最近の分子生物学の進歩，遺伝子改変マウスの開発，病理・組織学的研究の進展などにより，動脈硬化プラークの初期および進展時における生化学的，形態学的な変化に関する研究が進展している．そして，その結果，プラークの形成には，内膜への種々の細胞の取り込み，コレステロールの蓄積，マクロファージの泡沫化，線維性皮膜の形成，またプラークの破綻には，細胞外マトリックスの分解，血栓の形成などの多くのプロセスが関与することが明らかとなってきた（図1）．したがって，それぞれの段階に応じて適切なイメージングの標的分子が存在することになるので，診断，治療のための不安定プラークの分子イメージングには目的に応じて適切な分子プローブを選択することが必要と考えられる．例えば早期あるいは予防診断にはプラーク形成の初期段階に関与する分子，また，治療にはそれぞれの作用の対象となっている過程を評価できる分子を標的とすることが有効であり，場合によってはいくつかの分子プローブを組み合わせて用いることも必要であろう．

一方，不安定プラークの診断には，プラークの形成部位は小さいことから，形態学的に高い空間解像力をもち，かつその部位での質的変化をイメージングできる装置が必要である．最近，形態画像と機能画像を融合した画像を得ることのできる高感度，高解像力のPET/SPECT-CT，MRIなどのイメージング装置の開発が急速に進んでいる．したがって，このようなイメージング装置と，標的部位に特異的かつ高く集積する分子プローブの使用によって，血管内不安定プラークの分子イメージングによる質的診断が更に発展するものと期待される．

分子イメージングにより，不安定プラークをその破綻前に発見し，治療につなげていくことは心筋梗塞や脳血管障害などの疾患の発症前予防につながり，我が国における死亡率の大幅な減少にも大きく貢献するものと期待され，その発展が望まれている．

文献

1) Jaffer FA, Libby P, Weissleder R. Molecular and cellular imaging of atherosclerosis; emerging applications. J Am Coll Cardiol. 2006; 47: 1328-38.
2) Lindsay AC, Choudhury RP. Form to function: current and future roles for atherosclerosis imaging in drug development. Nat Rev Drug Discov. 2008; 7: 517-29.
3) Langer HF, Haubner R, Pichler BJ, et al. Radionuclide imaging. J Am Coll Cardiol. 2008; 52: 1-12.
4) Sadeghi MM, Glover DK, Lanza GM, et al. Imaging atherosclerosis and vulnerable plaque. J Nucl Med. 2010; 51: 51-65S.
5) Elkhawad M, Rudd JH. Radiotracer imaging of atherosclerotic plaque biology. Cardiol Clin. 2009; 27: 345-54.
6) Fox JJ, Strauss HW. One step closer to imaging vulnerable plaque in the coronary arteries. J Nucl Med. 2009; 50: 497-500.

7) Ogawa M, Ishino S, Mukai T, et al. ^{18}F-FDG accumulation in atherosclerotic plaques: immunohistochemical and PET imaging study. J Nucl Med. 2004; 45: 1245-50.
8) Rudd JHF, Myers KS, Bansilal S, et al. ^{18}Fluorodeoxyglucose positron emission tomography imaging of atherosclerotic plaque inflammation is highly reproducible. J Am Coll Cardiol. 2007; 50: 892-6.
9) Bural GG, Torigian DA, Chamroonrat W, et al. FDG-PET is an effective imaging modality to detect and quantify age-related atherosclerosis in large arteries. Eur J Nucl Med Mol Imaging. 2008; 35: 562-9.
10) Wykrzykowska J, Lehman S, Williams G, et al. Imaging of inflamed and vulnerable plaque in coronary arteries with ^{18}F-FDG PET/CT in patients with suppression of myocardial uptake using a low-carbohydrate, high-fat preparation. J Nucl Med. 2009; 50: 563-8.
11) Ogawa M, Magata Y, Kato T, et al. Application of [^{18}F]FDG-PET for monitoring the therapeutic effect of anti-inflammatory drugs on stabilization of vulnerable atherosclerotic plaques. J Nucl Med. 2006; 48: 1822-7.
12) Wu YW, Kao HL, Chen MF, et al. Characterization of plaques using ^{18}F-FDG PET/CT in patients with carotid atherosclerosis and correlation with matrix metalloproteinase-1. J Nucl Med. 2007; 48: 227-33.
13) Tahara N, Kai H, Yamagishi S, et al. Vascular inflammation evaluated by [^{18}F]-fluorodeoxyglucose positron emission tomography is associated with the metabolic syndrome. J Am Coll Cardiol. 2007; 49: 1533-9.
14) Tahara N, Kai H, Ishibashi M, et al. Simvastatin attenuates plaque inflammation: evaluation by fluorodeoxyglucose positron emission tomography. J Am Coll Cardiol. 2006; 48: 1825-31.
15) Lee SJ, On YK, Lee EJ, et al. Reversal of vascular ^{18}F-FDG uptake with plasma high-density lipoprotein elevation by atherogenic risk reduction. J Nucl Med. 2008; 49: 1277-82.
16) Matter CM, Wyss MT, Meier P, et al. ^{18}F-Choline images murine atherosclerotic plaques ex vivo. Arterioacler Thromb Vasc Biol. 2006; 26; 584-9.
17) Ishino S, Mukai T, Kume N, et al. Lectin-like oxidized LDL receptor-1 (LOX-1) expression is associated with atherosclerotic plaque instability-analysis in hypercholesterolemic rabbits. Atherosclerosis. 2007; 195: 48-56.
18) Ishino S, Mukai T, Kuge Y, et al. Targeting of lectinlike oxidized low-density lipoprotein receptor 1 (LOX-1) with ^{99m}Tc-labeled anti-LOX-1 antibody: potential agent for imaging of vulnerable plaque. J Nucl Med. 2008; 49: 1677-85.
19) Li D, Patel A, Klibanov A, et al. Molecular imaging of atherosclerotic plaques targeted on oxidized LDL receptor LOX-1 using SPECT/CT and magnetic resonance [abstract]. J Nucl Med. 2009; 50: 657.
20) Sarai M, Hartung D, Petrov A, et al. Broad and specific caspase inhibitor-induced acute repression of apoptosis in atherosclerotic lesions evaluated by radiolabeled annexin A5 imaging. J Am Coll Cardiol. 2007; 50: 2305-12.
21) Laufer EM, Winkens MHM, Narula J, et al. Molecular imaging of macrophage cell death for the assessment of plaque vulnerability. Arterioscler Thromb Vasc Biol. 2009; 29: 1031-8.
22) Nguyen QD, Smith G, Glaser M, et al. Positron emission tomography imaging of drug-induced tumor apoptosis with a caspase-3/7 specific [^{18}F]-labeled isatin sulfonamide. Proc Natl Acad Sci U S A. 2009; 106: 16375-80.
23) Ohshima S, Petrov A, Fujimoto S, et al. Molecular imaging of matrix metalloproteinase expression in atherosclerotic plaques of mice deficient in apolipoprotein E or low-density-lipoprotein receptor. J Nucl Med. 2009; 50: 612-7.
24) Zhang J, Nie L, Razavian M, et al. Molecular imaging of activated matrix metalloproteinase activity in the arterial wall in vivo. Circulation. 2008; 118: 1953-60.
25) Fujimoto S, Hartung D, Edward DS, et al. Molecular imaging of matrix metalloproteinase in atherosclerotic lesions: resolution with dietary modification and statin therapy. J Am Coll Cardiol. 2008; 52: 1847-57.
26) Tekabe Y, Qing L, Luma J, et al. Noninvasive monitoring the biology of atherosclerotic plaque development with radiolabeled annexin V and

matrix metalloproteinase inhibitor in spontaneous atherosclerotic mice. Circulation. 2009; 120 Suppl : S365-6.

27) Kuge Y, Takai N, Ishino S, et al. Distribution profiles of membrane Type-1 Matrix Metalloproteinase (MT1-MMP) , Matrix Metalloproteinase-2 (MMP-2) and cyclooxygenase-2 (COX-2) in rabbit atherosclerosis: comparison with plaque instability analysis. Biol Pharm Bull. 2007; 30: 1634-40.

28) Annovazz A, Bonanno E, Arca M, et al. ^{99m}Tc-interleukin-2 scntigraphy for the in vivo imaging of vulnerable atherosclerotic plaques. Eur J Nucl Med Mol Imaging. 2006; 33: 117-26.

29) Hartung D, Petrov A, Haider N, et al. Radiolabeled monocyte chemotactic protein 1 for the detection of inflammation in experimental atherosclerosis. J Nucl Med. 2007; 48: 1816-21.

30) van den Borne SWM, Isobe S, Verjans JW, et al. Molecular imaging of interstitial alterations in remodeling myocardium after myocardial infarction. J Am Coll Cardiol. 2008; 52: 2017-28.

31) Nahrendorf M, Zhang H, Hembrador S, et al. Nanoparticle PET-CT imaging of macrophages in inflammatory atherosclerosis. Circulation. 2008; 117: 379-87.

32) Cunningham CH, Arai T, Yang P, et al. Positive contrast magnetic resonance imaging of cells labeled with magnetic nanoparticles. Magn Reson Med. 2005; 53: 999-1005.

33) Dharmakumar R, Koktzoglou I, Li D. Generating positive contrast from off-resonant spins with steady-state free precession magnetic resonance imaging: theory and proof-of-principle experiments. Phys Med Biol. 2006; 51: 4201-15.

34) Mani V, Briley-Saebo KC, Itskovich VV, Set al. Gradient echo acquisition for superparamagnetic particles with positive contrast (GRASP) : sequence characterization in membrane and glass superparamagnetic iron oxide phantoms at 1.5T and 3T. Magn Reson Med. 2006; 55: 126-35.

35) Zurkiya O, Hu X. Off-resonance saturation as a means of generating contrast with superparamagnetic nanoparticles. Magn Reson Med. 2006; 56: 726-32.

36) Stuber M, Gilson WD, Schar M, et al. Positive contrast visualization of iron oxide-labeled stem cells using inversion-recovery with ON-resonant water suppression (IRON). Magn Reson Med. 2007; 58: 1072-7.

37) Korosoglou G, Tang L, Kedziorek D, et al. Positive contrast MR-lymphography using inversion recovery with ON-resonant water suppression (IRON). J Magn Reson Imaging. 2008; 27: 1175-80.

38) Korosoglou G, Weiss RG, Kedziorek DA, et al. Noninvasive detection of macrophage-rich atherosclerotic plaque in hyperlipidemic rabbits using "positive contrast" magnetic resonance imaging. J Am Coll Cardiol. 2008; 52: 483-91.

39) Winter P, Caruthers S, Zhang H, et al. Antiangiogenic synergism of integrin-targeted fumagillin nanoparticles and atorvastatin in atherosclerosis. J Am Coll Cardiol Imaging. 2008; 1: 624-34.

40) Cyrus T, Zhang H, Allen JS, et al. Intramural delivery of rapamycin with alphavbeta3-targeted paramagnetic nanoparticles inhibits stenosis after balloon injury. Arterioscler Thromb Vasc Biol. 2008; 28: 820-6.

Multimodal nonlinear optical imaging of atherosclerotic plaque development in myocardial infarction-prone rabbits

Alex C. T. Ko,[a,*] Andrew Ridsdale,[b] Michael S. D. Smith,[a] Leila B. Mostaço-Guidolin,[a] Mark D. Hewko,[a] Adrian F. Pegoraro,[b] Elicia K. Kohlenberg,[a] Bernie Schattka,[a] Masashi Shiomi,[c] Albert Stolow,[b] and Michael G. Sowa[a]

[a]National Research Council Canada, Institute for Biodiagnostics, 435 Ellice Avenue, Winnipeg, Manitoba, Canada R3B 1Y6
[b]National Research Council Canada, Steacie Institute for Molecular Sciences, 100 Sussex Drive, Ottawa, Ontario, Canada K1A 0R6
[c]Kobe University School of Medicine, Institute of Experimental Animals, 7-5-1, Kusunoki-cho, Chuo-ku, Kobe 650-0017, Japan

Abstract. Label-free imaging of bulk arterial tissue is demonstrated using a multimodal nonlinear optical microscope based on a photonic crystal fiber and a single femtosecond oscillator operating at 800 nm. Colocalized imaging of extracellular elastin fibers, fibrillar collagen, and lipid-rich structures within aortic tissue obtained from atherosclerosis-prone myocardial infarction-prone Watanabe heritable hyperlipidemic (WHHLMI) rabbits is demonstrated through two-photon excited fluorescence, second harmonic generation, and coherent anti-Stokes Raman scattering, respectively. These images are shown to differentiate healthy arterial wall, early atherosclerotic lesions, and advanced plaques. Clear pathological changes are observed in the extracellular matrix of the arterial wall and correlated with progression of atherosclerotic disease as represented by the age of the WHHLMI rabbits. © *2010 Society of Photo-Optical Instrumentation Engineers.* [DOI: 10.1117/1.3353960]

Keywords: atherosclerosis; nonlinear optical microscopy; photonic crystal fiber; coherent anti-Stokes Raman scattering; two-photon excited fluorescence; second harmonic generation.

Paper 09412LR received Sep. 18, 2009; revised manuscript received Jan. 27, 2010; accepted for publication Feb. 10, 2010; published online Mar. 12, 2010.

Atherosclerosis is the primary cause of heart disease, stroke, and lower limb amputation worldwide. It is a progressive disease characterized by chronic inflammation of injured intima and is associated with fatty plaque deposits in the arteries.[1,2] Early atherosclerosis cannot be reliably detected by current clinical methods, therefore the disease is often overlooked until at a more advanced stage. The development of new tools that provide greater sensitivity and specificity for early detection and differentiation of atherosclerotic plaques would help our understanding of early disease and help establish preventative regimens that would slow disease progression.

Recently, nonlinear optical (NLO) microscopy has emerged as a powerful tool for tissue imaging. It is a label-free method with high sensitivity and specificity for major extracellular molecules. Its optical sectioning capability presents a means of 3-D *in vivo* imaging that would be useful in the context of atherosclerosis diagnostics. Several studies have demonstrated imaging of arterial tissue using NLO microscopy,[3–6] including studies imaging atherosclerotic lesions using a multimodal coherent anti-Stokes Raman Scattering (CARS) microscope based on two tightly synchronized Ti:sapphire lasers and a swine animal model.[6,7] In our study, we demonstrate label-free visualization of the extracellular matrix of arterial lumen and atherosclerotic plaques using a photonic crystal fiber (PCF)-based multimodal NLO microscope employing only a single femtosecond oscillator. Two-photon excited autofluorescence (TPEF) is able to specifically image extracellular elastin fibers, second harmonic generation (SHG), type-1 collagen fibrils, and CARS lipid-rich structure or extracellular lipids droplets in unstained bulk intact tissue, indicating the methods are particularly suited to understanding the role and interplay between these key extracellular molecules involved in plaque development.

PCF-based CARS was recently reported as an alternative CARS imaging method in biology.[8,9] Because it only requires a single femtosecond laser, PCF-based CARS can be easily integrated into existing multiphoton microscopes with minimal reconfiguration, and provides CARS capability at a relatively low cost. Its portability and its future potential of being developed into an all-fiber, single-laser-based CARS imaging system are better than a conventional dual-color system. From a clinical research point of view, this CARS configuration is better adapted to being implemented in a surgical environment.

Colocalized elastin/type-1 collagen lipid imaging of bulk arterial tissues freshly harvested from WHHLMI rabbits is achieved at micron resolution using a home-built NLO microscope. The TPEF and SHG signals are obtained using the femtosecond pump pulses, with the CARS signal being generated by spatially and temporally overlapping the pump pulse with the Stokes pulse produced in a PCF that is synchronously pumped by the same femtosecond laser. Our goals in this study are to investigate the potential of a PCF-based multimodal NLO imaging system for bulk tissue imaging and for extracting biomorphological information related to atherosclerotic lesion development in myocardial infarction-prone rabbits.

Figure 1 illustrates our PCF-based multimodal NLO imaging system used in this study. A green-pumped Ti:sapphire oscillator (Tsunami, Spectra-Physics, Mountain View, California) is the laser source, and the output wavelength is centered at 800 nm with a pulse duration of 100 fs, an 80-MHz repetition rate, and average output power of 1 W. The femtosecond pulses from the Ti:sapphire oscillator first pass through a Faraday isolator and then a pair of GTI chirp mirrors (Layertec GmbH, Germany). These mirrors are used to compensate for the large group velocity dispersion (GVD) caused by the Faraday isolator. The femtosecond pulses are then split

*Address all correspondence to: Alex C.T. Ko. Tel: 204-984-4622; Fax: 204-984-5472; E-mail: alex.ko@nrc-cnrc.gc.ca

1083-3668/2010/15(2)/020501/3/$25.00 © 2010 SPIE

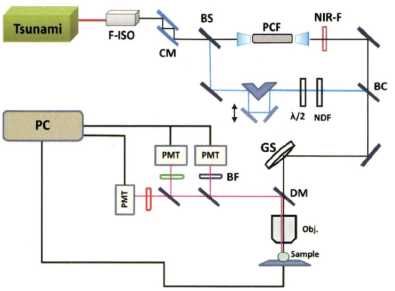

Fig. 1 Schematic of the inhouse-built nonlinear optical laser-scanning microscope with the Stokes pulses being generated in PCF, which is synchronously pumped by the same Ti:sapphire laser that provides the pump pulse. F-ISO: Faraday isolator; CM: chirp laser mirrors; BS: beamsplitter; NIR-F: near-IR filter; BC: beam combiner; GS: galvo scanner; DM: dichroic mirror; OBJ: objective lens; BF: bandpass filter; NDF: neutral density filter; and λ/2: half waveplate.

into two beams at a beamsplitter. The reflected "pump" pulse is transmitted through a series of optical components outlined in Fig. 1, while the transmitted pulse is coupled into a PCF (NL-1.4.775-945, NTK Photonics A/S, Denmark) through a 40× objective lens to generate a supercontinuum (SC). This SC emission is recollimated through a 20× objective lens and filtered through a near-infrared (NIR) filter to select only the NIR portion ($950\ \text{nm} < \lambda < 1150\ \text{nm}$), which is then used as the Stokes pulses for generating the CARS signal. The pump and Stokes pulses are combined at a beam combiner and sent collinearly into the microscope assembly. Epi-NLO signals are collected through an Olympus 20×, 0.75-NA objective lens (UPlanSApo) and then detected using nondescanned PMT modules (H-9656, Hamamatsu, Bridgewater, New Jersey). Spectral separation of TPEF, SHG, and CARS signals is achieved through an array of dichroic lenses and bandpass filters. A 40×, 0.8-NA, water immersion objective lens (Olympus LUMPlanFl/IR) is used to collect tissue images of greater spatial and depth resolution in selected regions of interest. Typically, 25 mW of pump and 8 mW of Stokes are used at the sample for imaging. ScanImage software[10] (Cold Spring Harbor Laboratory, New York) is used for image acquisition and controlling translational stage movement during depth imaging. For images shown, total pixel dwell time is 21 μs from an average of four scans. ImageJ ver 1.42b (National Institutes of Health, Bethesda, Maryland) is used for image viewing and post-processing.

Animal studies were approved by the local Animal Care Committee of the National Research Council of Canada. This study uses the myocardial infarction-prone Watanabe heritable hyperlipidemic (WHHLMI) rabbit model[11] which highly resembles human in lipoprotein metabolism compared to other models, and develops atherosclerotic plaques rapidly due to a hereditary defect in low-density lipoprotein processing. Seven WHHLMI rabbits were used for this study. Six rabbits were each sacrificed at 4, 10, 11, 16, 18, and 22 months, whereas the seventh rabbit died naturally at the age of 24 months. For each rabbit, fresh aorta was dissected from the ascending aorta to the external iliac artery, rinsed in heparinized saline,

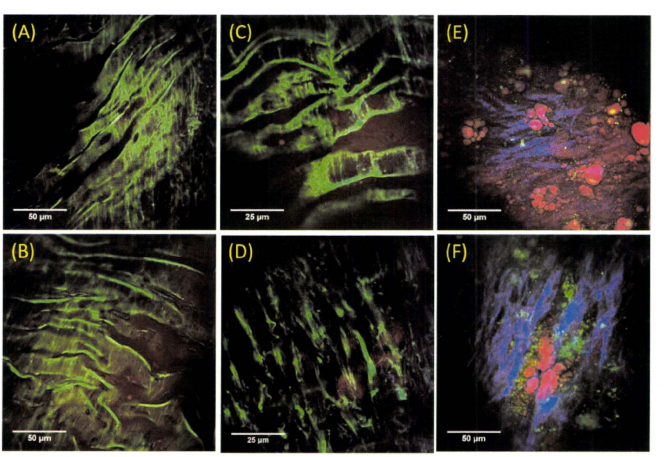

Fig. 2 Representative epi-NLO images collected from healthy arterial lumen on a (a) 4-month-old and (b) 10-month-old WHHLMI rabbit using 20× air objective lens, and on a 4-month-old rabbit using 40× WI lens at (c) lumen surface and (d) ~20 μm depth from surface. Representative epi-NLO images of arterial lumen surface obtained from (e) an early atherosclerotic lesion and (f) an advanced atherosclerotic lesion using 20× air lens. Green:TPEF (elastin or other fluorescent particles). Blue:SHG (collagen). Red:CARS (lipid-rich structure). (Color online only.)

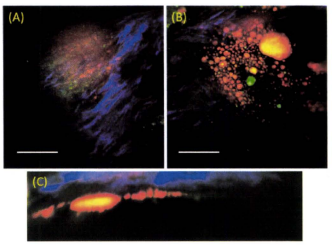

Fig. 3 Epi-NLO images of an advanced plaque obtained at (a) ~10 μm depth, (b) ~60 μm depth from the lumen surface, and (c) the side-view of the image stack showing a collagen cap overlaying lipid-rich bulk. Blue:SHG (collagen), and red/orange:CARS (lipid-rich structure). The scale bar is 25 μm. (Color online only.)

and then subdivided into ~20- to 30-mm sections. Each section was cut open longitudinally, exposing the luminal surface. The samples were placed in petri dishes with the luminal surface facing up. Phosphate buffered saline solution was applied to the samples periodically to maintain hydration. Healthier arterial lumen from the 4-month-old rabbit showed mostly smooth and flat surfaces with occasional raised lesions. Plaque-covered luminal surfaces were observed in rabbits aged 10 to 24 months with the burden increasing with age. This observation is consistent with the result reported on progressive atherosclerosis in the WHHLMI rabbits.[12]

Representative epi-NLO images of healthy luminal surfaces measured on 4- and 10-month-old rabbits are shown in Figs. 2(a) and 2(b), respectively. Near the surface of the vessel wall, a layer of membrane structure giving rise to strong TPEF signal (shown in green) is evident. At a depth of approximately 20 μm, a different fibril structure appears in the TPEF images with the orientation of these structural fibers running nearly perpendicular to that of the membrane layer detected closer to the surface. [Fig. 2(d)]. The membrane-shaped structure shown in Figs. 2(a)–2(c) is consistent with internal elastic lamina in arterial tunica intima, and the fibril structure shown in Fig. 2(d) is believed to be the bulk elastin network in arterial tunica media. A representative NLO image acquired from the surface of an early atherosclerotic lesion found on the arterial wall of the 10-month-old rabbit is illustrated in Fig. 2(e). Unlike in the images acquired from healthy luminal surfaces, no internal elastic lamina is visible. Instead, scattered collagen fibers, accumulated lipid-rich structures, and nonfibrous fluorescent structures emerged from the image. Images acquired from advanced plaque reveal lumen pathology similar to those of early lesions, with differences in collagen fibril morphology and denser systems of nonfibrous fluorescent structures. Older, more advanced plaques show thicker and directional collagen fibrils, as seen in Fig. 2(f), whereas early and midstage lesions show thinner and less directional collagen fibrils [Fig. 2(e)]. Figure 2(e) also shows the accumulation of extracellular lipid aggregates and the early formation of collagen fibrils within a lesion.

Depth scanning of an advanced plaque on a 22-month-old rabbit artery shows a thin collagen fibril layer overlaying a pool of lipid debris, a typical pathology of a rupture-prone atherosclerotic plaque. Figures 3(a) and 3(b) are two focal depth images obtained from the same location on an advanced plaque at depths approximately 10 and 60 μm respectively from the lumen surface. In Fig. 3(c) a reconstructed side-view image representing a depth profile of this particular plaque shows a collagen layer on top of a lipid-rich pool.

In conclusion, we demonstrated multimodal nonlinear optical imaging of bulk arterial tissue from WHHLMI rabbits using a cost-effective PCF-based nonlinear optical microscope. Epi-NLO imaging of unsectioned arteries allowed label-free visualization of extracellular components relevant to the development of atherosclerosis. Clear differences in the surface biochemical morphology were observed between healthy artery wall, early atherosclerotic lesions, and advanced plaques. In particular, differences in collagen fibril structures were noted between early and advanced lesions. Such changes in collagen morphology detected by SHG may provide a clinical measure for differentiating plaque burden.

Acknowledgment

The authors acknowledge Vijay Iyer for the assistance provided in using ScanImage, and Jeri Friesen for her assistance in preparing figures. This work was supported by the National Research Council Canada, Genomics and Health Initiative.

References

1. P. Libby, "Atherosclerosis: disease biology affecting the coronary vasculature," *Am. J. Cardiol.* **98**[suppl], 3Q–9Q (2006).
2. G. K. Hansoon, "Inflammation, atherosclerosis, and coronary artery disease," *N. Engl. J. Med.* **352**, 1685–1695 (2005).
3. A. Zoumi, X. Lu, G. S. Kassab, and B. J. Tromberg, "Imaging coronary artery microstructure using second-harmonic and two-photon fluorescence microscopy," *Biophys. J.* **87**(4), 2778–2786 (2004).
4. M. B. Lilledahl, O. A. Haugen, C. D. L. Davis, and L. O. Svaasand, "Characterization of vulnerable plaques by multiphoton microscopy," *J. Biomed. Opt.* **12**(4), 044005 (2007).
5. T. T. Le, I. M. Langohr, M. J. Locker, M. Sturek, and J. X. Cheng, "Label-free molecular imaging of atherosclerotic lesions using multimodal nonlinear optical microscopy," *J. Biomed. Opt.* **12**(5), 054007 (2007).
6. H. W. Wang, T. T. Le, and J. X. Cheng, "Label-free imaging of arterial cells and extracellular matrix using a multimodal CARS microscope," *Opt. Commun.* **281**, 1813–1822 (2008).
7. H. W. Wang, I. M. Langohr, M. Sturek, and J. X. Cheng, "Imaging and quantitative analysis of atherosclerotic lesions by CARS-based multimodal nonlinear optical microscopy," *Arterioscler., Thromb., Vasc. Biol.* **29**, 1342–1348 (2009).
8. A. F. Pegoraro, A. Ridsdale, D. J. Moffatt, Y. Jia, J. P. Pezacki, and A. Stolow, "Optimally chirped multimodal CARS microscopy based on a single Ti:sapphire oscillator," *Opt. Express* **17**(4), 2984–2996 (2009).
9. S. Murugkar, C. Brideau, A. Ridsdale, M. Naji, P. K. Stys, and H. Anis, "Coherent anti-Stokes Raman scattering microscopy using photonic crystal fiber with two closely lying zero dispersion wavelengths," *Opt. Express* **15**(21), 14028–14037 (2007).
10. T. A. Pologruto, B. L. Sabatini, and K. Svoboda, "ScanImage: flexible software for operating laser scanning microscopes," *Biomed. Eng. Online* **2**, 13 (2003).
11. M. Shiomi, T. Ito, S. Yamada, S. Kawashima, and J. Fan, "Development of an animal model for spontaneous myocardial infarction (WHHLMI rabbit)," *Arterioscler., Thromb., Vasc. Biol.* **23**, 1239 (2003).
12. T. Itp, S. Yamada, and M. Shiomi, "Progression of coronary atherosclerosis relates to the onset myocardial infarction in an animal model of spontaneous myocardial infarction (WHHLMI rabbits)," *Exp. Anim.* **53**, 339–346 (2004).

Neurourology and Urodynamics 29:1350–1354 (2010)

The Effects of Chronic Hyperlipidemia on Bladder Function in Myocardial Infarction-Prone Watanabe Heritable Hyperlipidemic (WHHLMI) Rabbits

Masaki Yoshida,[1]* Koichi Masunaga,[2] Takashi Nagata,[3] Yo Satoji and,[4] Masashi Shiomi[5]

[1]*Department of Urology, Kumamoto Hospital of Japan Labor Health and Welfare Organization, Kumamoto, Japan*
[2]*Department of Urology, Tokyo Metropolitan Geriatric Hospital, Tokyo, Japan*
[3]*Department of Urology, Toshiba Hospital, Tokyo, Japan*
[4]*Department of Urology, Graduate School of Medical Sciences, Kumamoto University, Kumamoto, Japan*
[5]*Institute for Experimental Animals, Kobe University School of Medicine, Kobe, Japan*

Aims: Lower urinary tract symptoms (LUTS) are common in the aging population. LUTS cause profoundly negative impacts on their quality of life. Pathophysiology of LUTS is multifactorial, and recently, bladder ischemia and metabolic syndrome have been suggested as etiological factors. To evaluate chronic hyperlipidemia on bladder function, we examined the functional and histological changes of the bladder in myocardial infarction-prone Watanabe Heritable Hyperlipidemic (WHHLMI) rabbits. **Methods:** 20- to 24-month-old WHHLMI rabbits and age- and sex-matched control rabbits were prepared. Bladder functions were evaluated using cystometrograms and functional experiments with isolated bladder specimens. Histological studies of bladder and internal iliac arteries were performed with hematoxylin and eosin staining. The bladder was also stained immunohistochemically with mouse monoclonal S-100 antibodies and sheep polyclonal calcitonin gene-related peptide (CGRP) antibodies. **Results:** In cystometric examination, WHHLMI rabbits showed significantly shorter micturition interval, smaller voided volume with non-voiding contractions, and lower micturition pressure, as compared to control. The functional experiments showed that carbachol- and electrical field stimulation-induced contractions were significantly decreased in WHHLMI rabbits than those in control. In WHHLMI rabbits, cross-sections of internal iliac arteries showed significant atherosclerosis and thickening of media. Bladder showed thinner urothelium and decreased smooth muscle area in WHHLMI rabbits, as compared to control. WHHLMI rabbits showed a significant decrease in S-100 protein positive neurons, and an increased number of CGRP positive neurons. **Conclusions:** This study demonstrated that WHHLMI rabbits showed detrusor overactivity with decreased detrusor contraction. It is suggested that chronic hyperlipidemia contributes to the bladder dysfunction. *Neurourol. Urodynam. 29:1350–1354, 2010.* © 2010 Wiley-Liss, Inc.

Key words: LUTS; hyperlipidemia; ischemia; WHHLMI rabbits

INTRODUCTION

Lower urinary tract symptoms (LUTS) are common symptoms in the aging population.[1,2] Many people receive profoundly negative impacts on their quality of life from LUTS. The pathophysiology of LUTS is multifactorial, and various etiological factors have been suggested. Recently, metabolic syndrome and bladder ischemia have been suggested as important etiological factors.[3,4] Hyperlipidemia is a well-known risk factor for development and progression for cardiovascular and metabolic diseases. However, association between LUTS and hyperlipidemia is less clear.

Several studies have suggested the changes in bladder function using high cholesterol fed animal with ligation or balloon injury of bladder arteries.[5–7] The reports demonstrated that moderate bladder ischemia caused detrusor overactivity and increase contractile response to carbachol and EFS with moderate fibrosis in the bladder wall, whereas the severe bladder ischemia caused very weak bladder contraction and decreased response to the stimulation.[6] In the experimental model, acute development of atherosclerosis and acute bladder ischemia were induced. Thus, it seems not to be appropriate model for the gradual development of atherosclerosis and ischemia, as it develops in human. Watanabe heritable hyperlipidemic (WHHL) rabbit has been developed as an animal model for human familial hypercholesterolemia and atherosclerosis at first,[8] and now a myocardial infarction-prone Watanabe Heritable Hyperlipidemic (WHHLMI) rabbit as its new strain has been widely used as a model of hyperlipidemia, various organ ischemia, and related diseases.[9–11] Therefore, WHHLMI rabbits might be suitable for evaluation of bladder dysfunction due to chronic hyperlipidemia and slowly progression of atherosclerosis.

In the present study, we examined the functional and histological changes of bladder of WHHLMI rabbits and evaluated the effects of chronic hyperlipidemia and slowly progression of atherosclerosis with bladder ischemia on bladder function.

Conflict of Interest: Yoshida-Consultant: Astellas Pharm., Kissei Pharm., Pfizer. Speaker Honorarium: Astellas Pharm., Kissei Pharm., Pfizer.
Lori Birder led the review process.
*Correspondence to: Masaki Yoshida, MD, Department of Urology, Kumamoto Hospital of Japan Labor Health and Welfare Organization, 3-30-34-1402, Suizenji, Kumamoto 862-0950, Japan. E-mail: akko-maki@umin.net
Received 16 August 2009; Accepted 12 October 2009
Published online 1 February 2010 in wileyonlinelibrary.com
DOI 10.1002/nau.20843

MATERIALS AND METHODS

Animals

This study was performed according to the Institutional Animal Care and Use in the Ethics Committee of Kumamoto University.

We prepared 20- to 24-month-old WHHLMI rabbits (n = 6), and age- and sex-matched Japanese white rabbits (n = 10) as controls. All WHHLMI rabbits were bred at and donated from the Institute of Experimental Animals of Kobe University School of Medicine. All rabbits were housed individually in metabolic cages in a room temperature and were fed standard rabbit chow (CR-3, Clea, Tokyo, Japan) and water ad libitum for 1 week. For evaluation of blood parameters, blood samples were taken from marginal ear vein after overnight fasting, and were referred to a commercial laboratory (SRL, Tokyo, Japan).

Evaluation of Bladder Function

The urine of each rabbit was automatically captured in a container under the cage, which was connected to an electronic pressure transducer (NA-021, Neuroscience, Tokyo, Japan). The frequency-volume chart (FVC) was recorded and monitored using an electronic pen recorder for 3 days. Then, the bladder was surgically exposed under anesthesia with sodium pentobarbital (35–50 mg/kg) and a catheter (OP-30-05, Eicom, Kyoto, Japan) was inserted into the bladder for cystometric examination, using constant infusion (1.0 ml/min) of saline into the bladder to elicit voiding. The catheter was connected to pressure transducer (TP-400T, Nihon-Kohden, Tokyo, Japan) for measurement of bladder pressure. Saline voided from urethral meatus was collected and measured to determine the voided volume, and the residual volume was measured by aspiration of the residual saline through the intravesical catheter, after the infusion was stopped at the beginning of a voided contraction. In our recording system, we determined bladder contractions over 4 cmH_2O as non-voiding contractions.

Functional Experiments

Under pentobarbital anesthesia, rabbits were sacrificed. Then, bladder was excised, and immersed in Krebs–Henseleit solution. Serosal layer was dissected and bladder strips were cut (approximately 2 mm wide and 8 mm long) from the dome of the bladder. The set up of the bladder specimen was performed as previously described.[12] The bladder strip was suspended in a 20-ml organ bath filled with Krebs–Henseleit solution. Then each preparation was connected to a force displacement transducer (TB-611T; Nihon-Kohden) and an isometric force was recorded and monitored on an ink-writing recorder. Concentration–response curves for carbachol were obtained by increasing the concentration in a stepwise manner after the response to the previous concentration had reached a plateau.

Contractile responses to 80 mM KCl were obtained by equimolar replacement of NaCl by KCl in Krebs–Henseleit solution. Electrical field stimulation (EFS) was generated between two parallel platinum wire electrodes (10 mm wide and 8 mm apart). Electrical impulses for field stimulation of the intramural nervous system of the strips were delivered with a stimulator (SEN-3301; Nihon-Kohden) and boosted by an amplifier (SEG-3104; Nihon-Kohden). The intrinsic nerves were stimulated with rectangular pulses of 0.3 msec duration and 40 V, at stimulation frequencies of 2–40 Hz. Trains of pulses lasted for 2 sec and there was an interval of 2 min between stimulations.

Histological Study

For the histological examination, bladders were fixed by immediate immersion in 0.2 M phosphate-buffered 4% paraformaldehyde (pH 7.4) at 4°C for 4–6 hr. After fixation, they were rinsed and cryoprotected with 10% sucrose in 0.01 M PBS at 4°C for 4 hr to overnight. The fixed specimens were dehydrated in graded ethanol and embedded in paraffin wax. Sections (5 μm) were cut, mounted onto precoated slides, and stained with hematoxylin and eosin (H&E) using standard methods.

To examine pathological changes of bladder vessels, distal portion of internal iliac arteries of two rabbits of both groups were also excised, sectioned transversely, and fixed and mounted onto slides. The prepared slides were stained with H&E.

Formaldehyde-fixed (4%) specimens of bladder in both WHHL (n = 6) and control (n = 10) rabbits were immunohistochemically stained for mouse monoclonal S-100 antibodies (Abcam, Cambridge, UK) and sheep polyclonal calcitonin gene-related peptide (CGRP) antibodies (Biogenesis, England, UK), as previously described.[13,14] During the staining procedure, the sections were pretreated with 3% H_2O_2 for 15 min to remove endogenous peroxidase activity from the tissue and immersed in a solution consisting of 1% bovine serum albumin, 5% NaCl, 1% gelatin, 0.15% glycine, and 1% Tween-20/100 ml of 20 mM Tris–HCl for 5 min to block non-specific background. The treated sections were exposed to the mouse monoclonal antibody S-100 or the sheep polyclonal antibody CGRP at 4°C for overnight. They were then exposed to the goat polyclonal antibody as a secondary antibody for primary antibody (DAKO, Copenhagen, Denmark) for 30 min. The reaction site was stained with diaminobenzidine and counter-stained with hematoxylin for 1 min. The sections were dehydrated through graded alcohols, cleared in xylene, and mounted.

All histological sections were examined using a microscope. A quantitative evaluation of the nerve density in the muscular and stromal layers was calculated, as previously described.[15] In brief, all separate nerve fibers and the constituting nerve fibers in each nerve bundle were counted. In this way, the total number of nerve fibers was obtained. After counting five fields, the mean nerve density score (MNDS) can be calculated.

Statistical Analysis

Values were expressed as mean ± SEM. Statistic analyses for comparisons between groups and between contraction curves were carried out using analysis of variance (ANOVA) and the Fisher's test. $P < 0.05$ was considered as a statistical significance.

RESULTS

There were no significant differences between WHHLMI and control rabbits in body weight, bladder weight, and blood serum examinations except total cholesterol and triglyceride level. Total cholesterol level (496 ± 58 mg/dl, n = 6) and triglyceride level (220.5 ± 22.5 mg/dl, n = 6) in WHHLMI rabbits were significantly higher, as compared to the control (19.5 ± 2.5 and 44.3 ± 4.4 mg/dl, respectively, n = 10). Examination of distribution of cholesterol revealed that WHHLMI rabbits showed three times higher amount of LDL fraction

than that of the control group (60.4 ± 2.8%, n = 6 and 19.2 ± 3.8%, n = 10, respectively).

In FCV, the number of micturition of WHHLMI rabbits (5.9 ± 0.9 times/day, n = 6) was significantly higher than that of the control (2.4 ± 0.6 times/day, n = 10), although the daily urinary volume (WHHLMI rabbits: 75.8 ± 9.3 ml, n = 6; control rabbits: 72.6 ± 10.4 ml, n = 10) was not different between groups. The micturition volume of the WHHLMI rabbits (16.0 ± 5.1 ml, n = 6) was significantly lower than that of the control (43.6 ± 6.9 ml, n = 10).

Typical recordings of the cystometric study in both groups are shown in Figure 1. The micturition volume was significantly lower, and micturition interval was significantly shorter in WHHLMI rabbits. WHHLMI rabbits also showed significantly lower micturition pressure. The post-voided residual urine did not show any significant differences in both groups (Table I).

In the functional study using bladder smooth muscle strips, 80 mM KCl-induced contractions of the control and WHHLMI rabbits (40.2 ± 8.0 mN, n = 10 and 37.6 ± 3.9 mN, n = 6, respectively) were not significantly different. As for carbachol- and EFS-induced contractions, the contractile response was showed as % of KCl-induced contraction. The concentration– and frequency–response curves for smooth muscle strips of WHHLMI rabbits showed substantially weaker contraction to the control (Fig. 2).

In the histological studies, the urothelium of WHHLMI rabbits was thinner than that of the control. Moreover, the amount of muscle fibers decreased and connective tissues increased in the WHHLMI rabbits. In WHHLMI rabbits, the cross-sections of distal portion of internal iliac arteries showed significant atherosclerosis lesions and thickening of media (Fig. 3).

Positive staining for the monoclonal antibody S-100 or the polyclonal antibody CGRP was indicated by red-brown color fibers in bladder of both groups. S-100 positive neurons were mainly detected in smooth muscles layer, and CGRP positive neurons were mainly detected in suburothelium (Fig. 4). WHHLMI rabbits showed significantly lower MNDS of S-100 positive neurons (14.5 ± 3.07, n = 6) and significantly higher MNDS of CGRP positive neurons (30.60 ± 5.43, n = 6), as compared to the control rabbits (29.50 ± 5.22 and 14.9 ± 3.00, n = 10, respectively).

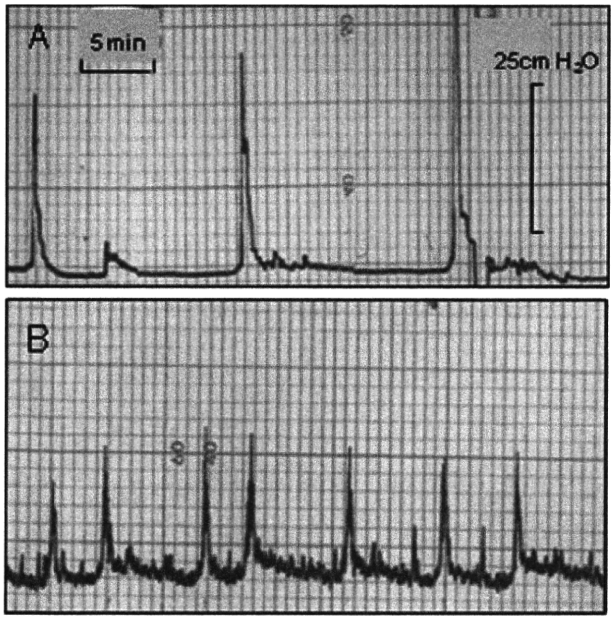

Fig. 1. Typical recordings of cystometrogram. **A**: Control rabbits; **B**: WHHLMI rabbits. WHHLMI rabbits showed shorter interval of micturition and lower micturition pressure, as compared to the control rabbits. There were non-voiding contractions in WHHLMI rabbits.

TABLE I. Comparison of Cystometic Findings Between the WHHLMI rabbits and the Control Group

	WHHLMI (n = 6)	Control (n = 10)
Micturition volume (ml)	6.82 ± 0.87*	20.8 ± 3.2
Interval of micturition (min)	4.52 ± 1.04*	13.87 ± 2.51
Micturition pressure (cmH_2O)	21.8 ± 2.1*	26.8 ± 2.3
Post void residual urine (ml)	1.20 ± 0.41	0.82 ± 0.23

Each value represents mean ± SEM. * $P < 0.05$; significantly different from the comparable value for control.
The bladder was surgically exposed under anesthesia with sodium pentobarbital, and a catheter was inserted into the bladder for cystometric examination, using constant infusion (1.0 ml/min) of saline into the bladder to elicit voiding. The catheter was connected to pressure transducer for measurement of bladder pressure. Saline voided from urethral meatus was collected and measured to determine the voided volume, and the residual volume was measured by aspiration of the residual saline through the intravesical catheter.

DISCUSSION

WHHLMI rabbits were developed as an animal model for myocardial infarction.[9,10] WHHLMI rabbits showed significant atherosclerotic lesions, and aortic atherosclerosis is observed grossly from 4-month old despite being fed normal chow, and the severity of atherosclerotic lesions increased significantly with aging.[9] WHHLMI rabbits are considered to be a good model for research on hyperlipidemia and atherosclerosis, and related ischemic diseases. Additionally, it has been reported that the lipid metabolism and the morphology of the atherosclerotic lesions of WHHLMI rabbits resemble those of humans.[9] Therefore, we used this model in the present experiment. The data of blood biochemistry in this study were consistent with the previous reports.[9–11]

It has been reported that 96% of the WHHLMI rabbits had cerebrovascular atherosclerosis. However, no rabbits showed involvement of penetrating arteries, and stenoses caused by cerebral atherosclerosis generally were milder than those associated with coronary or aortic atherosclerosis. Moreover, no behavioral or morphologic evidence of brain infarction were observed.[11] Hence, it is suggested that bladder dysfunction of WHHLMI rabbits observed in the present study may not be caused by apparent brain disorders. In the present study, we could not evaluate when bladder dysfunction started in WHHLMI rabbits. Evaluation for age-dependent changes of bladder function in WHHLMI rabbits will be needed to clarify it.

In FVC and cystometrogram, WHHLMI rabbits showed frequent voiding and detrusor overactivity (non-voiding contractions). However, micturition pressure of WHHLMI rabbits was significantly lower than that of control. In addition, the functional study with smooth muscle strips from WHHLMI rabbits showed the significantly decreased responses to carbachol and EFS, as compared to control. WHHLMI rabbits showed significant atherosclerosis lesions and thickening of media in the iliac arteries, suggesting slowly progression of ischemia of the bladder. Therefore, in WHHLMI rabbits, the chronic hyperlipidemia and/or atherosclerosis-

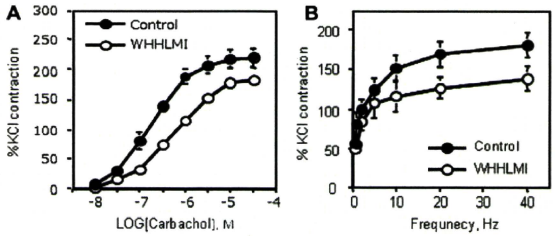

Fig. 2. Concentration–response curves to carbachol (**A**) and frequency–response curves to EFS (**B**) in the isolated detrusor smooth muscles of WHHLMI rabbits (○) **and the control rabbits (●). The contractile responses were showed as % of 80 mM KCl-induced contractions. Each point represents the mean ± SEM, if not shown, SEM bars fall within the size of the symbols.**

induced poor blood supply to bladder may be related to bladder dysfunction. It is interesting that the WHHLMI rabbits showed almost same results as rabbits with severe bladder ischemia reported by Azadzoi et al.[6] On the other hand, Shenfeld et al.[16] reported that gradual onset of atherosclerosis in apolipoprotein E gene knockout mice did not caused significant changes in bladder smooth muscle contractile responses to bethanechol, KCl, or resting tone. Although differences in the experimental animal and severity of atherosclerosis may contribute to the different results between the report and the present study, further studies will be required to clarify the reasons.

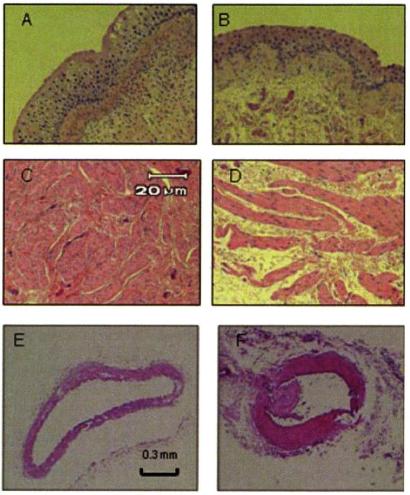

Fig. 3. Histological findings of the bladder and distal portion of internal iliac artery in the control (**A**,**C**,**E**) and WHHLMI (**B**,**D**,**F**) rabbits. The urothelium of WHHLMI rabbits (B) was thinner than that of the control (A), and smooth muscle area of WHHLMI rabbits (D) decreased with replacement by connective tissues. In WHHLMI rabbits, atherosclerosis lesions and thickening of media (F) were observed, as compared to the control (E).

WHHLMI rabbits showed a significant increase in CGRP positive neurons. CGRP is one of the predominant excitatory neurotransmitters in mediating sensory perception, and an important nociceptive marker.[17] CGRP has a major role in mediating hypersensitivity in many systems, including lower urinary tract.[18] The increased CGRP positive neurons in WHHLMI rabbits might cause the enhanced afferent activity, resulting in urinary frequency and detrusor overactivity. Nerve growth factor (NGF) seems to control, at least partly, survival and outgrowth of CGRP positive neurons through its tyrosine kinase receptor A. It has been reported that the increases in NGF and CGRP positive neurons have strong relationship with detrusor overactivity in spinal cord injured rats.[19] The same mechanism may contribute to the detrusor overactivity observed in WHHLMI rabbits. It is suggested that NGF distribution is related to the increase in CGRP positive neurons. Further evaluation will be needed in this point. On the contrary, WHHLMI rabbits showed a significant decrease of S-100 protein positive neurons (denervation), which may contribute to the decreased contractility of bladder smooth

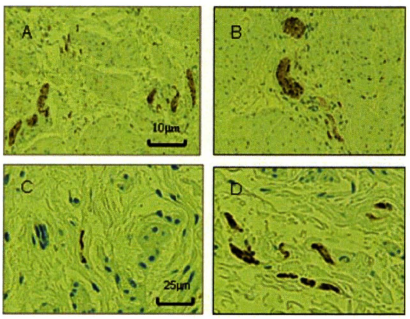

Fig. 4. Immunohistochemical stainings for S-100 positive neurons (**A**: control rabbits and **B**: WHHLMI rabbits) and CGRP positive neurons (**C**: control rabbits and **D**: WHHLMI rabbits). S-100 positive neurons were mainly found in smooth muscle layer, and CGRP-positive neurons mainly found under epithelium. Bladder of the WHHLMI rabbits showed smaller number of S-100 positive neurons (B) and greater number of CGRP positive neurons (D), as compared to the control rabbits (A,C).

muscles to stimulations. Although the mechanism of denervation is not fully understood, Ca^{2+}-dependent neutral protease calpain may be activated by ischemia and result in the proteolysis of neuronal membranes.[20] Histological study of bladder in WHHLMI rabbits showed the fibrosis of bladder wall and the decreased amount of detrusor smooth muscles, which may also contribute to the decreased bladder contractility.

The bladder dysfunction observed in WHHLMI rabbits might be described as the state of detrusor hyperactivity with impaired contraction which can be clinically experienced in human elderly. Although we did not evaluate the time-dependent changes in bladder function in WHHLMI rabbits, bladder dysfunction observed in this study might be a decompensate state after peripheral nervous system activated and reorganized to compensate hyperlipidemia and chronic ischemia with structural an functional changes of bladder. Azadzoi et al. suggested that severe bladder ischemia caused much severe fibrosis, which may be related to a significant increase in the expression of transforming growth factor beta-1 (TGF-β1), and that fibrosis might play a major role in bladder dysfunction.[5] They also speculated that detrusor overactivity observed in rabbits with moderate bladder ischemia was partly because of increased interstitial K^+ concentration in the detrusor, which was derived by decreased K^+ washout due to reduced blood flow.[6] They also suggested that lipoxygenase and cyclooxygenase pathways may affect bladder condition and that leukotrienes may overcome the effect of prostaglandin pathway under ischemic state, resulting in detrusor overactivity.[7]

The unique point in the present study is that bladder weight did not increase and bladder urothelium became thinner; whereas in other experimental models such as BOO, spinal cord injured, and bladder ischemia, bladder weight increased and urothelium appeared thickened, edematous and hyperemic.[5–7,20–22] In addition to the difference in urothelium compensation processes in the various experimental conditions, the presence and degree of inflammation or metabolic changes related to hyperlipidemia may account for urothelium thinning observed in the WHHLMI rabbits, although serum hyperlipidemia alone seems not to cause epithelium thinning.[5,23] Another possibility is the effects of oxidative stress. Reactive oxygen and reactive nitrogen species are known to be generated by ischemia, and they could damage the membrane function.[21] Those changes might promote mucosa thinning and increased permeability of urothelium as well as denervation in bladder wall. Further studies will be needed to clarify this point.

Recent study on WHHLMI rabbits has been shown that the combination of an inhibitor of an acyl-CoA: cholesterol *O*-acyltransferase inhibitor (avasimibe) to a statin (atrovastatin) is able to prevent progression and induce regression of established atherosclerotic lesions.[24,25] Furthermore, it has been reported that control of hyperlipidemia with statins inhibits the progression of kidney disease.[26] Therefore, it might be possible to apply those medicines to retard progression of LUTS or even reduce them. In addition, such study may clarify the mechanism of bladder dysfunction induced by chronic hyperlipidemia and slowly progression of atherosclerosis with bladder ischemia.

CONCLUSIONS

This study demonstrated that WHHLMI rabbits showed detrusor overactivity with decreased detrusor contractility. It is suggested that chronic hyperlipidemia contributes to bladder dysfunction and pathophysiology of LUTS. Furthermore, WHHLMI rabbits may be a useful model for evaluation of pathophysiology of LUTS and exploration of future treatment possibilities.

REFERENCES

1. Homma Y, Yamaguchi O, Hayashi K, The Members of the Neurogenic Bladder Society Committee. An epidemiological survey of overactive bladder symptoms in Japan. BJU Int 2005;96:1314–8.
2. Reeves P, Irwin D, Kelleher C, et al. The current and future burden and cost of overactive bladder in five European countries. Eur Urol 2006;50:1050–7.
3. Rahman NU, Phonsombat S, Bochinski D, et al. An animal model to study lower urinary tract symptoms and erectile dysfunction: The hyperlipidaemic rat. BJU Int 2007;100:658–63.
4. Lee WC, Chien CT, Yu HJ, et al. Bladder dysfunction in rats with metabolic syndrome induced by long-term fructose feeding. J Urol 2008;179:2470–6.
5. Azadoi KM, Tarcan T, Siroky M, et al. Atherosclerosis-induced chronic ischemia causes bladder fibrosis and non-compliance in the rabbit. J Urol 1996;161:1626–35.
6. Azadzoi KM, Tarcan T, Kozlowski R, et al. Overactivity and structural changes in the chronically ischemic bladder. J Urol 1999;162:1768–78.
7. Azadzoi KM, Shinde VM, Tarcan T, et al. Increased leukotriene and prostaglandin release, and overactivity in the chronically ischemic bladder. J Urol 2003;169:1885–91.
8. Watanabe T. Serial inbreeding of rabbits with hereditary hyperlipidemia (WHHL-rabbit). Atherosclerosis 1980;36:261–8.
9. Shiomi M, Ito T, Yamada S, et al. Development of an animal model for spontaneous myocardial infarction (WHHLMI rabbit). Arterioscler Thromb Vasc Biol 2003;23:1239–44.
10. Shiomi M, Fun J. Unstable coronary plaques and cardiac events in myocardial infarction-prone Watanabe heritable hyperlipidemic rabbits: Questions and quandaries. Curr Opin Lipidol 2008;19:631–6.
11. Ito T, Shiomi M. Cerebral atherosclerosis occurs spontaneously in homozygous WHHL rabbits. Atherosclerosis 2001;156:57–66.
12. Yoshida M, Homma Y, Inadome A, et al. Age-related changes in cholinergic and purinergic neurotransmission in human isolated bladder smooth muscles. Exp Gerontol 2001;36:99–109.
13. Ferrandino I, Grimaldi MC. S-100-immunoreactive nerves in the urinary bladder of the rat. Eur J Histochem 1995;39:127–32.
14. Collins JJ, Wilson K, Fischer-Colbrie R, et al. Distribution and origin of secretoneurin-immunoreactive nerves in the female rat uretus. Neuroscience 2000;95:255–64.
15. Van Poppel H, Stessens R, Baert L, et al. Endoscopic biopsies for quantitative nerve density evaluation of the urinary bladder. Eur Urol 1988;14:236–9.
16. Shenfeld OZ, Meir KS, Yutkin V, et al. Do atherosclerosis and chronic bladder ischemia really play a role in detrusor dysfunction of old age? Urology 2005;65:181–4.
17. Robinson DR, Gebhart GF. Inside information—The unique features of visceral sensation. Mol Interv 2008;8:242–53.
18. Vizzard MA. Alterations in neuropeptide expression in lumbosacral bladder pathways following chronic cystitis. J Chem Neuroanat 2001;21:125–38.
19. Zinck ND, Rafuse VF, Downie JW. Sprouting of CGRP primary afferents in lumbosacral spinal cord precedes emergence of bladder activity after spinal injury. Exp Neurol 2007;204:777–90.
20. Zhao Y, Levin SS, Wein AJ, et al. Correlation of ischemia/reperfusion on partial outlet obstruction-induced spectrin proteolysis by calpain with contractile dysfunction in rabbit bladder. Urology 1997;49:293–300.
21. Juan YS, Lin WY, Kalorin C, et al. The effect of partial bladder outlet obstruction on carbonyl and nitrotyrosine distribution in rabbit bladder. Urology 2007;70:1249–53.
22. Masunaga K, Yoshida M, Inadome A, et al. Prostaglandin E_2 release from isolated bladder strips in rats with spinal cord injury. Int J Urol 2006;13:271–6.
23. Son H, Lee SL, Park WH, et al. New unstable bladder model in hypercholesterolemia rats. Urology 2007;69:186–90.
24. Shiomi M, Ito T, Tsukada T, et al. Combination treatment with troglitazone, an insulin action enhancer, and pravastatin, an inhibitor of HMG-CoA reductase, shows a synergistic effect on atherosclerosis of WHHL rabbits. Atherosclerosis 1999;142:345–53.
25. Worthley SG, Helft G, Corti R, et al. Statin therapy alone and in combination with an acyl-CoA:cholesterol *O*-acyltransferase inhibitor on experimental atherosclerosis. Pathophysiol Haemost Thromb 2007;36:9–17.
26. Fried LF. Effects of HMG-CoA reductase inhibitors (statins) on progression of kidney disease. Kidney Int 2008;100:658–63.

Jpn J Radiol (2010) 28:656–662
DOI 10.1007/s11604-010-0487-0

ORIGINAL ARTICLE

Utility of contrast-enhanced ultrasonography for qualitative imaging of atherosclerosis in Watanabe heritable hyperlipidemic rabbits: initial experimental study

Ayumi Nitta-Seko · Norihisa Nitta · Masashi Shiomi Akinaga Sonoda · Shinichi Ota · Keiko Tsuchiya Masashi Takahashi · Mineko Fujimiya · Kiyoshi Murata

Received: January 15, 2010 / Accepted: July 7, 2010

Abstract
Purpose. Using Watanabe heritable hyperlipidemic (WHHL) rabbits, we investigated the ability of ultrasonography (US) to detect contrast enhancement of atherosclerotic lesions after intravenous injection of a microbubble contrast agent (MB) and confirmed the localization of MB in the lesion by transmission electron microscopy (TEM).
Materials and methods. The abdominal aortic wall of six WHHL rabbits was observed for 20 min after MB delivery. To evaluate contrast enhancement, a region of interest (ROI) was set in the intima–media complex (IMC) and the aortic lumen. The average image brightness of the ROI was recorded as the echogenicity at each time point. Differences at each time point were analyzed by analysis of variance and the *t*-test. Histological analysis was performed after US observation.
Results. The echogenicity of the IMC was 8.48 ± 3.01 before and 10.96 ± 7.88, 32.42 ± 12.79, 24.55 ± 8.01, 17.73 ± 9.18, and 31.18 ± 13.35, respectively, at 0.5, 2, 5, 10, and 20 min after MB injection. The echogenicity of the vessel lumen was 1.16 ± 1.57, 64.21 ± 11.52, 53.59 ± 9.81, 13.32 ± 9.78, 2.63 ± 1.45, and 3.66 ± 3.01 at the corresponding time points. At 20 min after injection, the echogenicity of the IMC was significantly higher than before or 0.5 min after injection. The distribution of MB inside macrophages in atherosclerotic plaques could not be confirmed by TEM.
Conclusion. Ultrasonography was able to detect contrast enhancement of the IMC at 10 and 20 min after injection of MB.

Key words Ultrasonography contrast agent · Sonazoid · Macrophage · Vasa vasorum · Atherosclerosis

A. Nitta-Seko (✉) · N. Nitta · A. Sonoda · S. Ota · K. Tsuchiya · M. Takahashi · K. Murata
Department of Radiology, Shiga University of Medical Science, Tsukinowa-cho, Seta, Otsu 520-2192, Japan
Tel. +81-77-548-2288; Fax +81-77-544-0986
e-mail: sekoayumi@yahoo.co.jp

M. Shiomi
Institute for Experimental Animals, Kobe University School of Medicine, Kobe, Japan

M. Fujimiya
Department of Anatomy 2, Sapporo Medical University, Sapporo, Japan

Introduction

As it is difficult to identify most lesions responsible for acute coronary syndrome (ACS) or stroke by their morphological features (e.g., size, degree of vascular stenosis), the focus of previous studies was their instability.[1,2] Therefore, reliable morphological and qualitative evaluation methods are needed prior to the occurrence of events.

The intravenous (IV) ultrasonography (US) microbubble contrast agent (MB) Sonazoid is available for clinical use. As the MB enters Kupffer cells via phagocytosis, the signal intensity of the normal hepatic parenchyma increases; and lesions such as hepatocellular carcinoma (HCC) and metastatic liver tumors can be visualized by relative signal-intensity differences.[3,4]

Unlike stable plaques, most unstable plaques are rich in macrophages and are considered a high risk for ACS.[5] We posited that if MB could be directed into the atherosclerotic lesion to be phagocytosed by resident macrophages this technique would constitute a highly useful

tool for the qualitative diagnosis of atherosclerotic lesions.

We used Watanabe heritable hyperlipidemic (WHHL) rabbits to determine whether US can detect contrast enhancement of atherosclerotic lesions after IV injection of MB and checked the localization of the MB in the lesions by transmission electron microscopy (TEM).

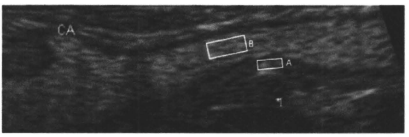

Fig. 1. Region of interest (ROI) settings in the rabbit vascular wall (*A*) and lumen (*B*). *CA*, celiac artery

Materials and methods

Sonazoid (Daiichi Sankyo, Tokyo, Japan) is a solution containing lipid-stabilized MB filled with perfluorobutane gas. The average particle diameter is 2–3 μm, and the MB concentration is 1×10^9 MB/ml. We injected 0.12 μl MB/kg (0.015 ml/kg), the dose recommended specifically for clinical liver studies.[3]

Animals

Six 26- to 30-week-old WHHL rabbits (4 males, 2 females) weighing 3–4 kg were randomly selected. One 26-week-old male rabbit was the control. WHHL rabbits have been used for the evaluation of atherosclerotic lesions in a number of earlier studies.[2,6–10] All experiments were approved by our Animal Care and Use Committee and carried out according to the Guidelines for Animal Experimentation at our institution.

Ultrasonography studies

A clinical US system (Aplio XG; Toshiba Medical Systems, Tokyo, Japan) with a 12-MHz linear convex probe (PLT1202S; Toshiba Medical Systems) was used. The rabbits were deprived of food for 24 h before the experiments. They were anesthetized with an intramuscular injection of a mixture of ketamine hydrochloride 25 mg/kg (Ketalar 50; Sankyo Yell Yakuhin, Tokyo, Japan) and medetomidine hydrochloride 0.1 mg/kg (Domitor; Meiji Seika, Tokyo, Japan). Prior to MB infusion, the abdominal aorta was studied by fundamental B-mode imaging, and the celiac and superior mesenteric arteries were identified on sagittal views (Fig. 3a). The probe was then fixed in that position to observe the aortic wall.

Contrast enhancement was observed on harmonic B-mode pulse subtraction images. The frame rate was set at 10 frames/s (FPS) and the mechanical index at 0.2, as the pulse subtraction (PS)-low mode. After recording prestudy images in the PS-low mode, a bolus injection of MB was delivered via the auricular vein. US scanning was at 0.5, 2, 5, 10, and 20 min after MB delivery. An image acquired at 0.5 min after injection was the first-pass image of the IV-injected MB. Images obtained at other time points were used to monitor US signal changes. The aorta of a rabbit not injected with MB was the control.

Image analysis

During each observation period, US images were recorded digitally and analyzed offline with image processing software (Photoshop CS4 extended; Adobe Systems, San Jose, CA, USA). To evaluate contrast enhancement, a region of interest (ROI) was set at just below the boundary of the media adventitia and at the center of the aortic lumen (Fig. 1). The average image brightness of the ROI, defined as the videodensity,[4] of the aortic lumen and aortic wall was compared. We used 10 × 100 pixels and measured two data points in the aortic wall and lumen.

Histology for light microscopy and TEM

Abdominal aorta specimens from the WHHL rabbits were fixed in phosphate-buffered glutaraldehyde and paraformaldehyde and embedded in paraffin to obtain 5-μm serial transverse tissue sections. We used Mallory-Azan, elastica van Gieson (EVG), and hematoxylin and eosin (H&E) staining for general morphological analysis. For immunohistochemical staining we used a monoclonal antibody to RAM11 (1:500) (Dako, Glostrup, Denmark) as a primary antibody against macrophages.

A portion of the aorta and liver was embedded in gelatin, and 50 μm thick slices were cut on a vibratome (Microslicer DTK-3000W; Dosaka, Kyoto, Japan). The sections were dehydrated in a graded series of ethanol, embedded in aqueous acrylic resin (LR gold resin; London Resin, London, UK),[11–13] and polymerized in an ultraviolet cryo chamber (Pelco; Ted Pella, Redding, CA, USA) at −20°C. Thick polymerized sections were first examined to select the appropriate area for ultrastructural study under a phase-contrast light microscope (Diaphot TMD300; Nikon, Tokyo, Japan). Ultra-thin 70-nm sections were then prepared in an ultramicrotome

(Ultracut UCT; Leica, Vienna, Austria). Staining was with uranyl acetate and lead citrate for the TEM study (H-7500; Hitachi, Tokyo, Japan). Control specimens were obtained from one WHHL rabbit not injected with MB. An original solution of Sonazoid, prepared according to the above procedure, was used for the TEM study.

Statistical analysis

Differences in US signals from the vessel lumen and wall before and after MB injection were analyzed by analysis of variance (ANOVA) and Tukey's HSD correction. Differences between the vessel lumen and wall at each time point were analyzed with the *t*-test. $P < 0.05$ was considered significant. SPSS version 11.0 (SPSS, Chicago, IL, USA) was used for all analyses.

Results

US Images

The video-density in the aortic wall (intima–media complex, or IMC) acquired in PS-low mode was 8.48 ± 3.01 before MB injection and 10.96 ± 7.88, 32.42 ± 12.79, 24.55 ± 8.01, 17.73 ± 9.18, and 31.18 ± 13.35 at 0.5, 2, 5, 10, and 20 min, respectively, after MB injection. At the corresponding time points, the video-densities from the aortic lumen were, respectively, 1.16 ± 1.57, 64.21 ± 11.52, 53.59 ± 9.81, 13.32 ± 9.78, 2.63 ± 1.45, and 3.66 ± 3.01 (Fig. 2).

With the exception of the adventitia, under PS-low mode the US signals from the IMC and aortic lumen were almost undetectable prior to the injection of MB (Fig. 3b). At 0.5 min after injection, high echogenic MB was observed in the arterial lumen ($P < 0.05$) (Fig. 3c); and a linear, low-signal zone corresponding to the IMC was recognized. The video-density from the vessel lumen decreased after 5 min ($P < 0.05$), and a dot-like (or linear) high-echoic signal appeared at the IMC (Fig. 3d). The video-density of the IMC was significantly higher at 2 and 20 min after MB injection than before and 0.5 min afterward. There was no significant difference in the video-density of the IMC before and 5 or 10 min after injection. At 10 and 20 min after injection there was a significant difference between the video-density of the IMC and the lumen ($P < 0.05$).

Histology and immunohistochemistry

The aortic wall in all WHHL rabbits was clearly atherosclerotic. Large, raised intimal lesions with lipid cores were evident. They were acellular, comprised of lipid-rich debris including cholesterol clefts, and surrounded by a layer of foam cells. Many lipid-laden foam cells were also seen in the subendothelium (Fig. 4).

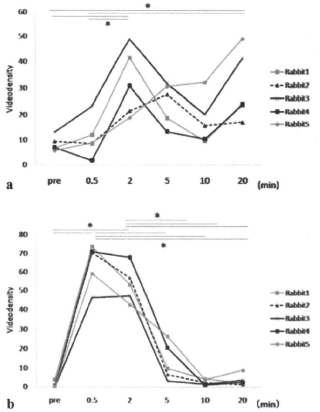

Fig. 2. Video-density of the aorta in rabbits. **a** Video-density of the aortic wall (intima–media complex, IMC). At 30 s after intravenous (IV) injection of the microbubble contrast agent (MB), the IMC appeared as a low-signal area. Before and 0.5 min after MB injection, the video-density of the IMC was almost the same. At 2 min after injection the video-density of the IMC peaked; it then decreased at 5–10 min after MB delivery. However, at 20 min after injection the video-density of the IMC was significantly higher than before and 0.5 min after injection. **b** Video-density of the aortic lumen. At 0.5–2.0 min after MB injection, the video-density of the aortic lumen showed a significant increase. At 5 min it began to decrease; the decline in video-density continued until it reached the preinjection level. $*P < 0.05$

The TEM revealed round 1- to 5-μm diameter particles distributed mainly in the lipid core[14] (Fig. 5a) that were similar to those present in the original solution (Fig. 5b). No MB was detected inside macrophages or in the capillary vessel lumen of the vasa vasorum.

Discussion

Atherosclerotic lesions in adult WHHL rabbits were evaluated using a US contrast agent. The US signal intensity (video-density) of the IMC was significantly higher at 20 min after MB injection than before or 0.5 min afterward. At 10 and 20 min after injection, the video-density of the IMC was significantly higher than that of the lumen. We attribute this to the contrast enhancement enabled by MB. At 10 or 20 min after

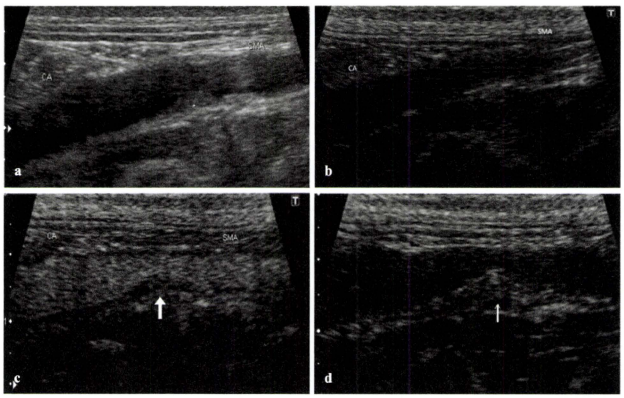

Fig. 3. Ultrasonography images. **a** Fundamental B-mode. **b** Before MB injection. It is difficult to identify the atherosclerotic lesions. **c** At 0.5 min after injection. High echogenic microbubbles are observed in the aortic lumen. **d** At 20 min after injection. Linear, high-echoic signals (*arrow*) appeared gradually on the surface of the IMC. **b–d** Harmonic B-mode pulse subtraction images. *CA*, celiac artery; *SMA*, superior mesenteric artery; *IMC*, intima–media complex

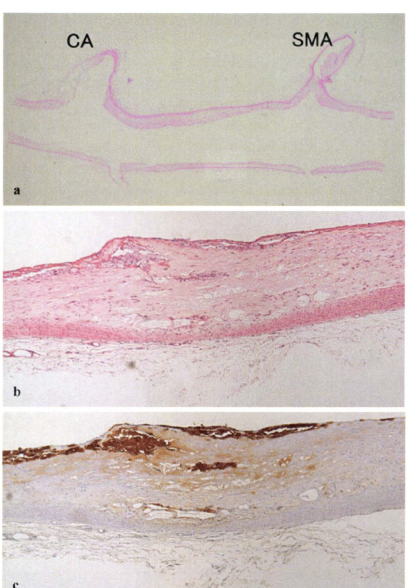

Fig. 4. Histological specimens of the rabbit abdominal aorta. **a** Loupe view. **b**, **c** ×40. **a**, **b** H&E stain. **c** Immunohistochemical stain (RAM11). The aortic wall shows evidence of atherosclerosis. Many RAM11-positive cells are seen in the plaque

injection there was little MB in the vessel lumen. We posit that contrast enhancement at these time points reflects the distribution of MB throughout the extravascular space. The video-density of the IMC was also significantly higher at 2 min after MB injection than before or 0.5 min afterward. The 2-min period corresponds to the vascular phase. We posit that our findings are indicative of the presence of MB in the capillary vessel lumen of the vasa vasorum because much MB persisted in the lumen at 2 min after injection.

We attribute the observed aortic wall enhancement to the presence of MB. TEM confirmed the presence of round structures, similar to those identified on TEM images of the original solution, in the extracellular matrix near the lipid core. Therefore, we considered the structures observed by TEM in the atherosclerotic plaques to be MB. All atherosclerotic lesions harbored abundant macrophages; they were always found in the subendothelium and around the plaque core. However, TEM identified no foam cells containing phagocytized MB. At 10 and 20 min after MB injection, the video-density of the lumen was lower than that of the IMC, suggesting that contrast-enhanced US imaging is useful for detecting vulnerable plaques. Ours is the first in vivo documentation of these phenomena in atherosclerotic lesions.

Sonazoid, an MB solution that is stable during US,[3,4] was developed to obtain consistent contrast enhancement on US images. Its properties are useful for early and delayed enhancement. Early enhancement reflects contrast-enhancing effects attributable to the intravascular presence of MB (the vascular phase). The agent

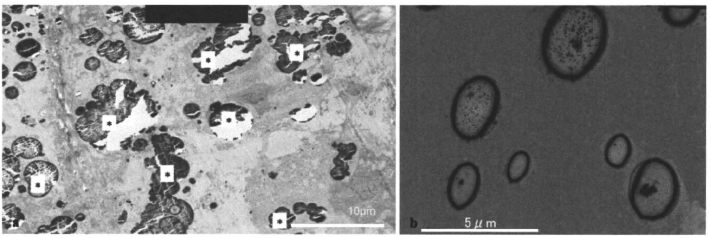

Fig. 5. Transmission electron microscopy study. **a** Note the round structures, thought to be MB, in the plaque core (*asterisks*). **b** Original Sonazoid solution. (**a** ×3000; **b** ×6000)

gradually disappears from the blood circulation and is incorporated into the reticuloendothelial system (RES). Furthermore, as the MB is phagocytosed by Kupffer cells, delayed (Kupffer) imaging is useful for detecting liver tumors in clinical US studies.[15–17]

We consider the round bodies shown in Fig. 5a to be MB because as in the original Sonazoid solution, the spheres were 2–3 μm in diameter, their surface was smooth, and their internal structure was uniform. Contrary to earlier reports,[18,19] our findings indicate that the 2- to 3-μm MB were able to migrate into atherosclerotic plaques.

The mechanisms underlying the migration of MB into vessels remain unclear. Although the intercellular gaps are wider between activated endothelial cells than in normal tissue, they are too narrow for the permeation by large particles such as Sonazoid.

The inner third of the aortic wall is fed by the blood flow and the outer two-thirds by the vasa vasorum from the adventitia side.[20] Although the normal vasa vasorum does not allow leakage, in the presence of atherosclerotic lesions it becomes permeable owing to the release of angiogenic factors such as vascular endothelial growth factor (VEGF). Because some newly generated vessels lack periocytes, various plasma components, including inflammatory cells, can leak out.[21] We used TEM to confirm that the identified structures were MB. As these structures were present in the extracellular matrix of the plaque core of MB-injected rabbits, we posit that MB leaked out of the vessels through the fragile vasa vasorum from the outside of the adventitia of the atherosclerotic artery.

Ultrasonography studies using MB contrast medium documented intraplaque neovascularization in carotid arteries.[21–24] Those studies assessed early enhancement to evaluate the degree of neovascularization as the level of angiogenesis represents a useful prognostic factor. By prolonging the observation time to include the delayed enhancement phase, we found that delayed contrast enhancement of the plaque recurred after the vascular phase, a phenomenon we attribute to vascular MB leakage. We consider our observations to be evidence of the fragility of the vessels. We also contend that our conclusion that MB is present in the capillary vessel lumen of the vasa vasorum and in the macrophages is not compromised by our observing only a small part of atherosclerotic lesions by TEM.

Various contrast agents used for the qualitative imaging of atherosclerotic lesions[25] reached the lesions and were extravasated by blood vessels. Nanoparticles such as ultra-small superparamagnetic iron oxide (USPIO)[10,26] and gadofluorine[9] have been used for magnetic resonance imaging, and N1177[27] has been used for CT studies. Others[28–30] reported using radioisotopes with a lower molecular weight, and some employed surface-modified MB with antibodies targeted at the endothelium.[31–33] The MB in those earlier reports remained attached only to the endothelial cell surface, and the presence of MB within the plaque core remained to be confirmed.

The clinical applicability of MB for purposes other than the detection of liver tumors varies.[16] The high echogenicity of Sonazoid administered IV may be useful for identifying vulnerable plaques. Our observations may lead to advances in the prognostic evaluation of atherosclerosis, and they may help in the assessment of the therapeutic effects of antilipidemic agents in patients with atheromatous plaques.[34]

Our study has some limitations. First, the optimal MB dose remains to be determined; the dose of Sonazoid we delivered was the one recommended for the diagnosis of human hepatic disease. Second, the detection sensitivity of US contrast enhancement was not sufficiently high for a precise diagnosis of the degree of atherosclerosis.

The most important diagnostic target is the coronary artery. To improve the quality of US images, further technological advances in image processing are necessary, as are better probes to detect echo signals from smaller targets.

Conclusion

In WHHL rabbits, prolonged contrast enhancement of the IMC was detected by US 10 and 20 min after MB injection.

Acknowledgments. We thank Mr. Takefumi Yamamoto (Central Research Laboratory, Shiga University of Medical Science) for technical assistance with the TEM. We also thank Mr. Yoshinori Saeki for excellent technical assistance with the histological specimens. This work was supported by a grant from the Japan Radiological Society in 2008 and received the silver medal at the annual meeting.

References

1. Van der Meer IM, Bots ML, Hofman A, del Sol AI, van der Kuip DA, Witteman JC. Predictive value of noninvasive measures of atherosclerosis for incident myocardial infarction: the Rotterdam Study. Circulation 2004;109:1089–94.
2. Shiomi M, Ito T, Yamada S, Kawashima S, Fan J. Correlation of vulnerable coronary plaques to sudden cardiac events: lessons from a myocardial infarction-prone animal model (the WHHLMI rabbit). J Atherosclerosis Thrombosis 2004;11: 184–9.
3. Watanabe R, Matsumura M, Chen CJ, Kaneda Y, Fujimaki M. Characterization of tumor imaging with microbubble-based ultrasound contrast agent, sonazoid, in rabbit liver. Biol Pharm Bull 2005;28:972–7.
4. Watanabe R, Matsumura M, Chen CJ, Kaneda Y, Ishihara M, Fujimaki M. Gray-scale liver enhancement with Sonazoid (NC100100), a novel ultrasound contrast agent; detection of hepatic tumors in a rabbit model. Biol Pharm Bull 2003;26:1272–7.
5. Moreno PR, Falk E, Palacios IF, Newell JB, Fuster V, Fallon JT. Macrophage infiltration in acute coronary syndromes: implications for plaque rupture. Circulation 1994;90:775–8.
6. Shindo J, Ishibashi T, Yokoyama K, Nakazato K, Ohwada T, Shiomi M, et al. Granulocyte-macrophage colony-stimulating factor prevents the progression of atherosclerosis via changes in the cellular and extracellular composition of atherosclerotic lesions in Watanabe heritable hyperlipidemic rabbits. Circulation 1999;99:2150–6.
7. Liang J, Liu E, Yu Y, Kitajima S, Koike T, Jin Y, et al. Macrophage metalloelastase accelerates the progression of atherosclerosis in transgenic rabbits. Circulation 2006;113: 1993–2001.
8. Shiomi M, Yamada S, Ito T. Atheroma stabilizing effects of simvastatin due to depression of macrophages or lipid accumulation in the atheromatous plaques of coronary plaque-prone WHHL rabbits. Atherosclerosis 2005;178:287–94.
9. Barkhausen J, Ebert W, Heyer C, Debatin JF, Weinmann HJ. Detection of atherosclerotic plaque with gadofluorine-enhanced magnetic resonance imaging. Circulation 2003;108: 605–9.
10. Kooi ME, Cappendijk VC, Cleutjens KB, Kessels AG, Kitslaar PJ, Borgers M, et al. Accumulation of ultrasmall superparamagnetic particles of iron oxide in human atherosclerotic plaques can be detected by in vivo magnetic resonance imaging. Circulation 2003;107:2453–8.
11. Fujimiya M, Okumiya K, Nakazawa M, Kitahama K, Kimura H, Maeda T. Effect of reserpine on 5-hydroxytryptophan (5HTP)-immunoreactive neurons in the rat brain. Histochemistry 1994;101:21–6.
12. Okumiya K, Matsubayashi K, Maeda T, Fujimiya M. Change in subcellular localization of gastrin-like immunoreactivity in epithelial cells of rat duodenum induced by carbachol. Peptides 1996;17:225–32.
13. Fujimiya M, Okumiya K, Kuwahara A. Immunoelectron microscopic study of the luminal release of serotonin from rat enterochromaffin cells induced by high intraluminal pressure. Histochem Cell Biol 1997;108:105–13.
14. Giuriato L, Scatena M, Chiavegato A, Zanellato AM, Guidolin D, Pauletto P, et al. Localization and smooth muscle cell composition of atherosclerotic lesions in Watanabe heritable hyperlipidemic rabbits. Arterioscler Thromb 1993;13:347–59.
15. Yanagisawa K, Moriyasu F, Miyahara T, Yuki M, Iijima H. Phagocytosis of ultrasound contrast agent microbubbles by Kupffer cells. Ultrasound Med Biol 2007;33:318–25.
16. Cosgrove D, Blomley M. Liver tumors: evaluation with contrast-enhanced ultrasound. Abdom Imaging 2004;29:446–54.
17. Hatanaka K, Kudo M, Minami Y, Ueda T, Tatsumi C, Kitai S, et al. Differential diagnosis of hepatic tumors: value of contrast-enhanced harmonic sonography using the newly developed contrast agent, Sonazoid. Intervirology 2008; 51(suppl 1):61–9.
18. Bartlett DW, Su H, Hildebrandt IJ, Weber WA, Davis ME. Impact of tumor-specific targeting on the biodistribution and efficacy of siRNA nanoparticles measured by multimodality in vivo imaging. Proc Natl Acad Sci U S A 2007;104:15549–54.
19. Greish K. Enhanced permeability and retention of macromolecular drugs in solid tumors: a royal gate for targeted anticancer nanomedicines. J Drug Targeting 2007;15:457–64.
20. Kumar V, Abbas AK, Fausto N, Mitchell RN. The blood vessels. In: Kumar V, Abbas AK, Fausto N, Mitchell RN, editors. Robbins basic pathology. 2007, pp 339–41. Philadelphia: Saunders Elsevier; 2007.
21. Feinstein SB. Contrast ultrasound imaging of the carotid artery vasa vasorum and atherosclerotic plaque neovascularization. J Am Coll Cardiol 2006;48:236–43.
22. Coli S, Magnoni M, Sangiorgi G, Marrocco-Trischitta MM, Melisurgo G, Mauriello A, et al. Contrast-enhanced ultrasound imaging of intraplaque neovascularization in carotid arteries: correlation with histology and plaque echogenicity. J Am Coll Cardiol 2008;52:223–30.
23. Vicenzini E, Giannoni MF, Puccinelli F, Ricciardi MC, Altieri M, Di Piero V, et al. Detection of carotid adventitial vasa vasorum and plaque vascularization with ultrasound cadence contrast pulse sequencing technique and echo-contrast agent. Stroke 2007;38:2841–3.
24. Shah F, Balan P, Weinberg M, Reddy V, Neems R, Feinstein M, et al. Contrast-enhanced ultrasound imaging of atherosclerotic carotid plaque neovascularization: a new surrogate marker of atherosclerosis? Vasc Med 2007;12:291–7.
25. Sanz J, Fayad ZA. Imaging of atherosclerotic cardiovascular disease. Nature 2008;451:953–7.
26. Ruehm SG, Corot C, Vogt P, Cristina H, Debatin JF. Ultrasmall superparamagnetic iron oxide-enhanced MR imaging of atherosclerotic plaque in hyperlipidemic rabbits. Acad Radiol 2002;9(suppl 1):S143–4.